# Supporting Information

## Dual-Functional Nanoengineering *via* Molecular Pillaring and Conductive Hybridization for High-Performance Aqueous Zinc-Ion Batteries

*Yajiang Wang[a b], Xiudong Chen[a] *, Jin-Hang Liu[a], Dongmei Qi[a b], Hai-Yan Hu[c], Huixiong Jiang[a], Yan Huang[b]*, Ping Yan[a], Yao Xiao[c d e]**

[a] School of Chemistry and Chemical Engineering, Jiangxi Province Engineering Research Center of Ecological Chemical Industry, Jiujiang University, Jiujiang 332005, China

[b] State Key Laboratory of Organic-Inorganic Composites, Beijing University of Chemical Technology, Beijing 100029, China

[c] College of Chemistry and Materials Engineering, Wenzhou University, Wenzhou, Zhejiang 325035, China

[d] State Key Laboratory of Powder Metallurgy, Central South University, Changsha 410083, China

[e] State Key Laboratory of New Textile Materials and Advanced Processing, Wuhan Textile University, Wuhan 430200, China

## Experimental Section

*Materials:* All reagents were of analytical grade and could be used without further purification. Ammonium vanadate ($NH_4VO_3$), Oxalic acid ($H_2C_2O_4 \cdot 2H_2O$), Tetra Methyl Ammonium Bromide ($C_4H_{12}BrN$, TMAB), graphene oxide (GO), Poly (vinylidene difluoride) (PVDF), acetylene black (AB), zinc trifluoromethanesulfonate ($Zn(CF_3SO_3)_2$) were purchased from Titan Scientific Co., Ltd., Shanghai, China.

*Synthesis of TNVO@GO:* $NH_4VO_3$ (0.64 g) and $H_2C_2O_4 \cdot 2H_2O$ (1.16 g) were dissolved in deionized water (40 mL), and then heated to 60 ℃ for stirring for 30 minutes. In another beaker, TMAB (0.2311 g) was dissolved in 20 mL of deionized water. Subsequently, $NH_4VO_3$ solution was added to the TMAB solution, with 5 mL (2 mg/mL) of GO added simultaneously. After stirring for 30 minutes, the mixture was transferred into a 100 mL Teflon-lined stainless steel autoclave and heated at 120 °C for 24 h. After cooling to room temperature, the product was washed repeatedly with deionized water and ethanol, followed by overnight drying at 60 °C to obtain TNVO@GO. Without TMAB, NVO was synthesized using the same procedure and conditions. Meanwhile, TNVO was synthesized using the same procedure and conditions without GO.

**Materials characterizations***:* The structure and morphology of the synthesized materials were characterized by X-ray diffractometer (XRD, Malvern Panalytical), FTIR (Bruker VERTEX70, 4000-400 $cm^{-1}$ region) and electron microscopes (SEM, S4800; TEM, Tecnai G2 F 20). Raman spectra were collected with a laser Raman spectrometer (HORIBA XploRA PLUS). The specific surface area and pore size distribution were studied through a Micromeritics TriStar Ⅱ 3020. X-ray photoelectron spectrometer (K-ALPHA 0.5EV) was utilized to evaluate the cathode material. The annealing process for the synthesized materials was investigated using a thermal

analyzer (America TA TGA55) in $O_2$. The unpaired electrons induced by oxygen vacancies in the material were detected by EPR (Bruker ELEXSYS-II E500).

***Electrochemical measurements****:* The CR2032 coin cells were assembled with as-prepared cathodes, 100 μm Zn foil anodes, glass fiber separators, and 2 M $Zn(CF_3SO_3)_2$ electrolyte. Cathodes were fabricated by mixing active materials, acetylene black, and NMP-dissolved PVDF solution at an 8:1:1 mass ratio, coated onto Ti foil, and dried at 60 °C for 12 h (mass loading: ~1.7 mg $cm^{-2}$). The LAND-CT3004A system was used to measure specific capacity, GCD performance, rate capability, cycling stability, and GITT (a current density of 0.1 A $g^{-1}$ with a relaxation time of 15 min). Moreover, CV (0.1-1.0 mV $s^{-1}$ scan rates, 0.2-1.6 V) and EIS measurements were carried out on a CHI760E electrochemical workstation. *Ex situ* XRD measurements and *in situ* Raman measurements were all conducted at a current density of 0.2 A $g^{-1}$ (0.2-1.6 V). Battery kinetics were analyzed *via* CV tests at different scan rates. The peak current scan rate correlation is as follows:

$$i = av^b \quad (1)$$

$$\log(i) = b\log(v) + \log(a) \quad (2)$$

where $i$ is the peak current, $v$ is the scan rate, and a and b are adjustable parameters. The value of b can be obtained by fitting the CV data using Equation. The capacitive contribution can be quantified using the following formula:

$$i(v) = k_1v + k_2v^{1/2} \quad (3)$$

where $k_1v$ is the current under capacitive control and $k_2v^{1/2}$ is the current under diffusion control. The diffusion coefficient of $Zn^{2+}$ ions is determined using the GITT method, and the formula is as follows:

$$D_{Zn^{2+}} = 4/\pi\tau \times (m_B V_m / M_B S)^2 (\Delta Es/\Delta E_\tau)^2 \quad (4)$$

where $D_{Zn^{2+}}$ represents the diffusion coefficient of zinc ions, $\tau$ is the relaxation time, $m_B$ is the mass loading of the active material, $V_m$ is the molar volume, $M_B$ is the molecular weight, S is the surface area of the active material, and $\Delta E_S$ and $\Delta E_t$ are the voltage changes caused by current pulses during charging and discharging, and the voltage change of the constant current pulse, respectively.

***First-Principles Calculations****:* This study employed density functional theory (DFT) calculations with the CASTEP module. Based on the generalized gradient approximation (GGA), structural optimization, single-point energy calculations, and electronic property computations of the material model were all executed using the Perdew-Burke-Ernzerhof (PBE) exchange-correlation energy functional. The double numerical plus polarization (DNP) basis set was selected, and core electrons were treated via DFT semi-core pseudopotential (DSPP) to lower computational overhead. To ensure computational results, energy and force convergence criteria were fixed at $10^{-5}$ Hartree (Ha) and 0.02 eV/Å, respectively. For structural optimization and density of states (DOS) calculations, the Monkhorst-Pack k-point mesh was set to 3×3×1 and 6×6×1, respectively.

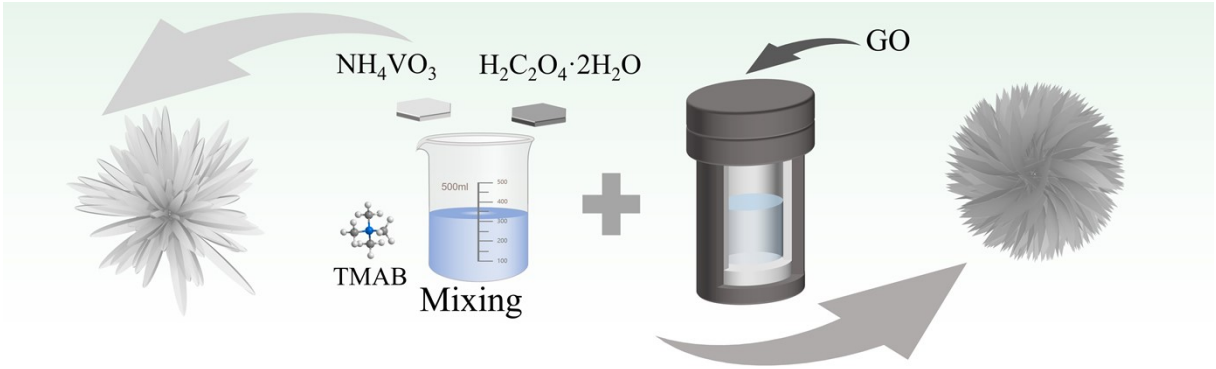


**Fig. S1.** Schematic illustration of the synthesis process of TNVO@GO.

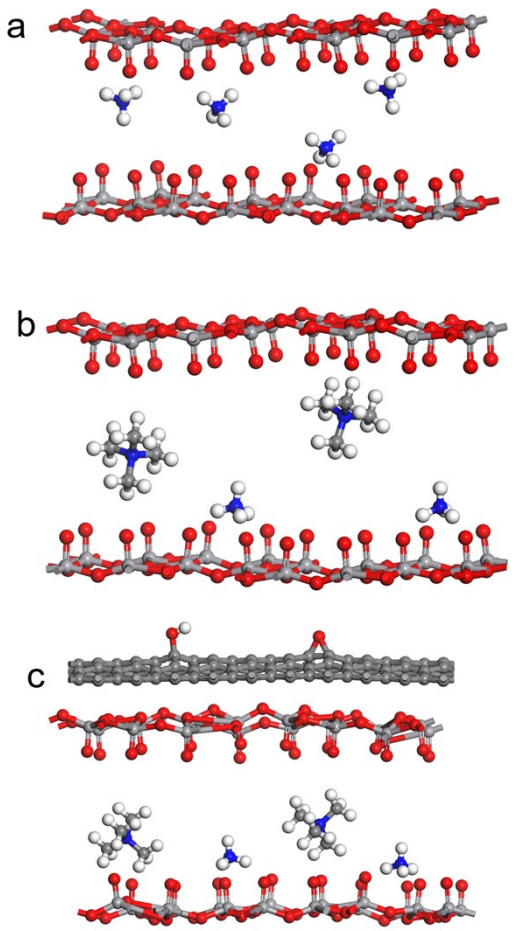


**Fig. S2.** The crystal structures of the (a) NVO, (b) TNVO, and (c) TNVO@GO.

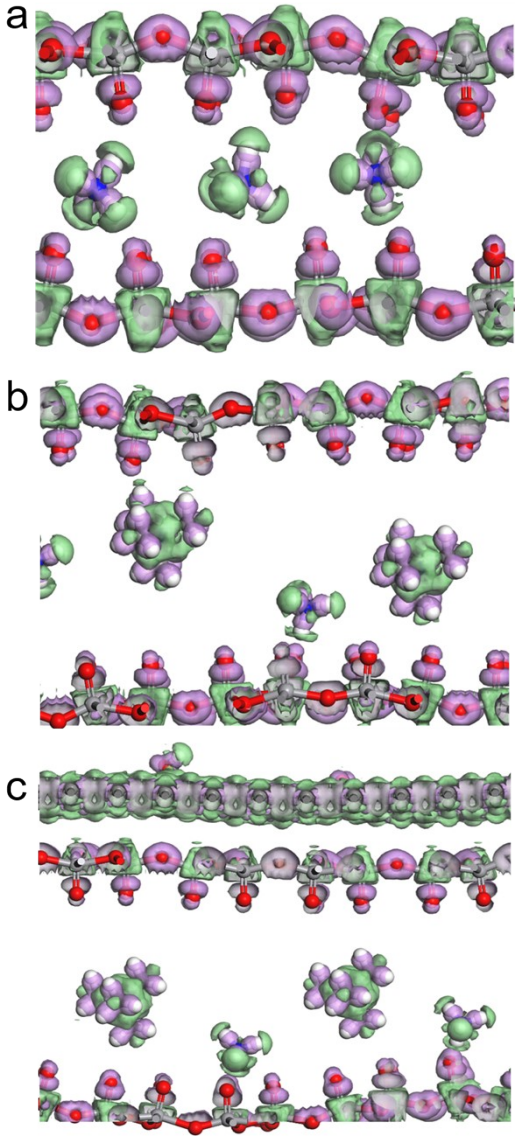


**Fig. S3.** Differential Charge Density of (a) NVO, (b) TNVO, and (c) TNVO@GO.

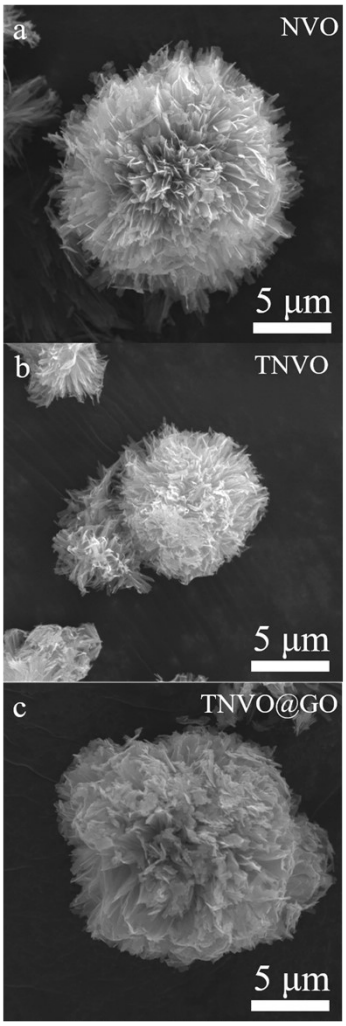


**Fig. S4.** SEM images of (a) NVO, (b) TNVO, and (c) TNVO@GO.

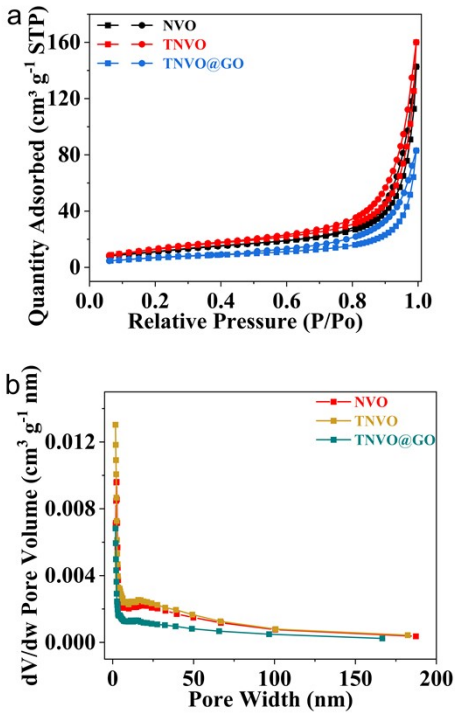


**Fig. S5.** (a) $N_2$ adsorption/desorption isotherms and (b) the pore size distribution of NVO, TNVO, and TNVO@GO.

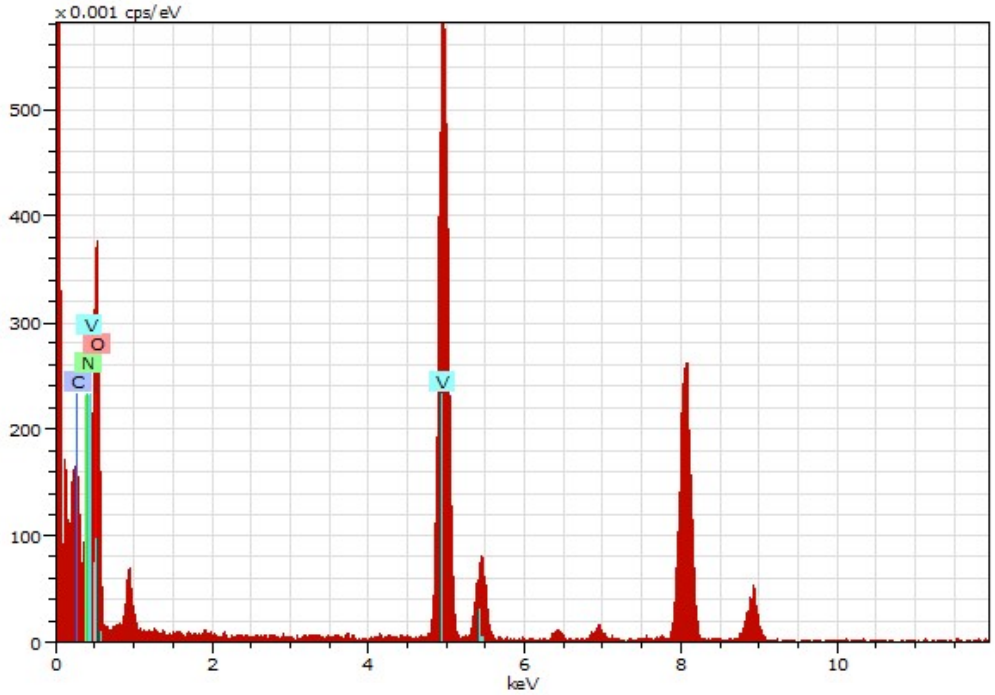


**Fig. S6.** The elemental mapping of TNVO@GO.

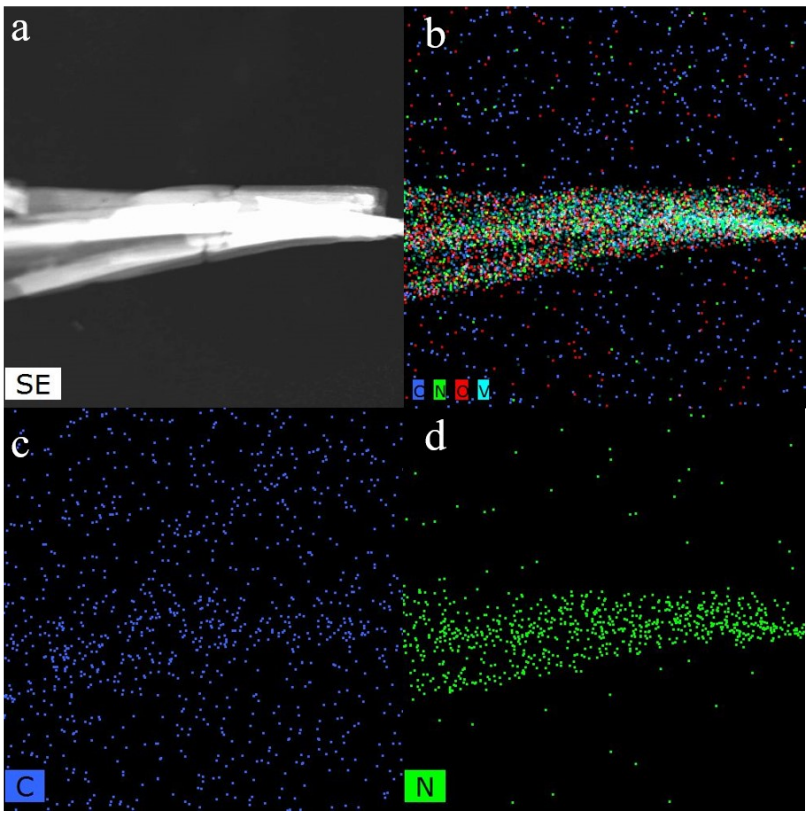


**Fig. S7.** The HAADF image and the corresponding elemental mappings of TNVO@GO.

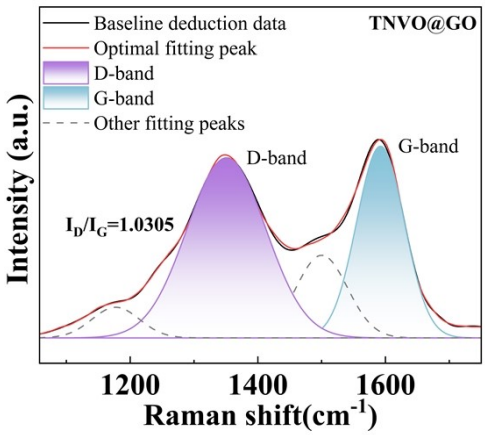


**Fig. S8.** Analysis of the Degree of Graphitization of TNVO@GO.

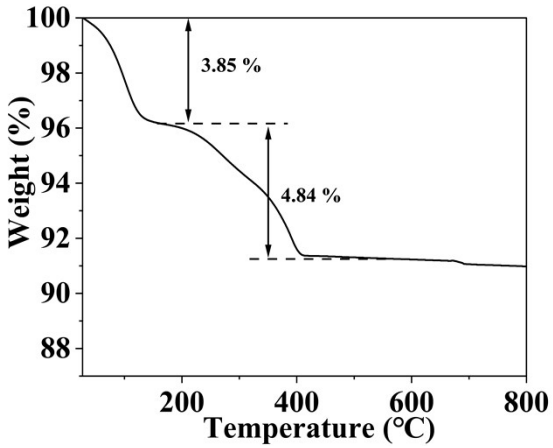


**Fig. S9.** TG curves of TNVO.

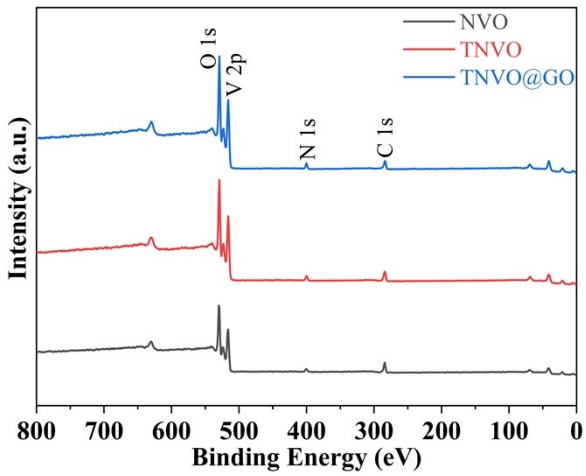


**Fig. S10.** The survey XPS spectrum of NVO, TNVO, and TNVO@GO.

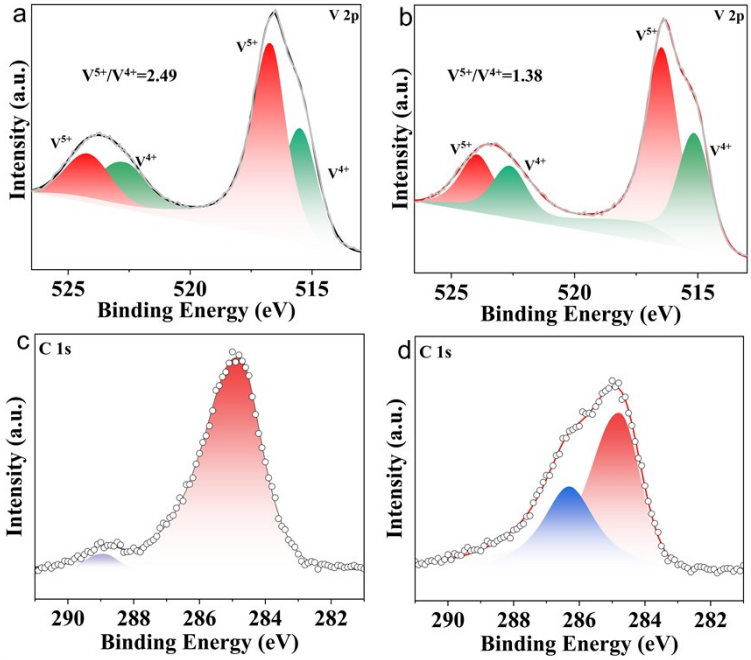


**Fig. S11.** The V 2p spectra of (a) NVO and (b) TNVO. The C 1s spectra of (c) NVO and (d) TNVO.

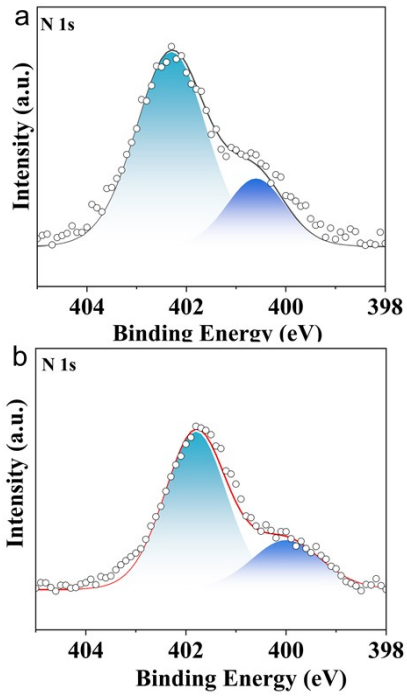


**Fig. S12.** The N 1s spectra of (a) NVO and (b) TNVO.

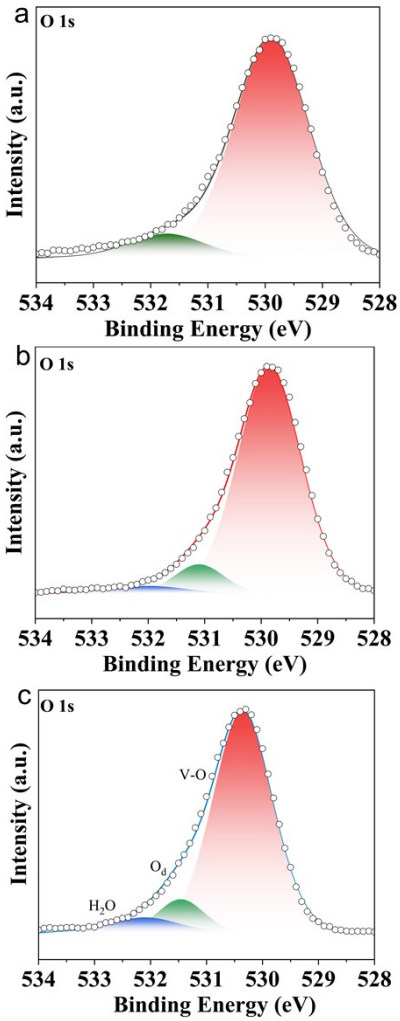


**Fig. S13.** The O 1s spectra of (a) NVO, (b) TNVO, and (c) TNVO@GO.

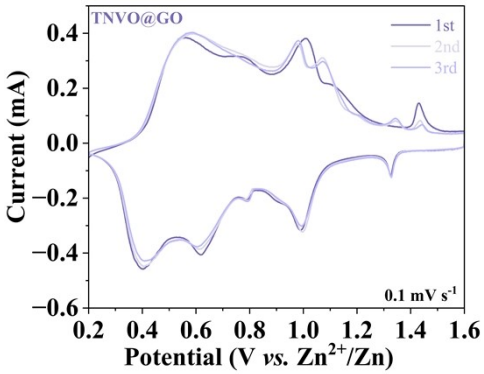


**Fig. S14.** The CV curves of TNVO@GO for the first three cycles at 0.1 mV $s^{-1}$.

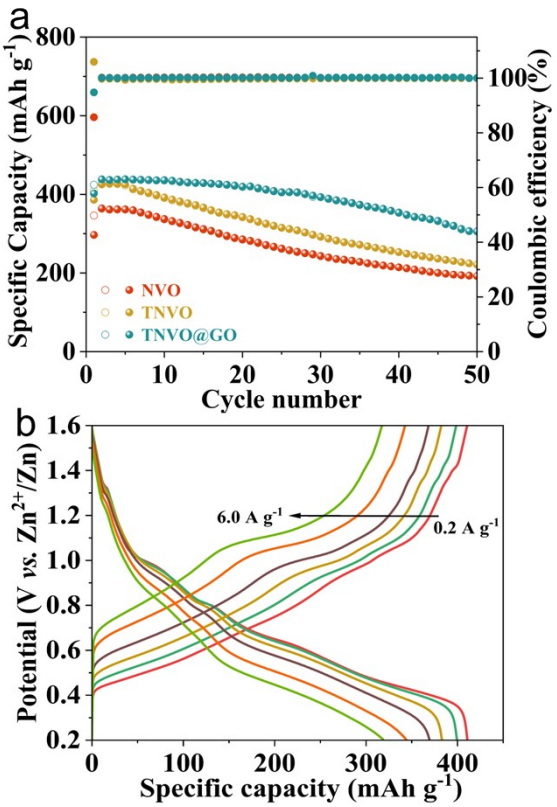


**Fig. S15.** (a) The Cycling performance at current density of 0.2 A $g^{-1}$. (b) The discharge and charge profiles at various current densities of TNVO@GO.

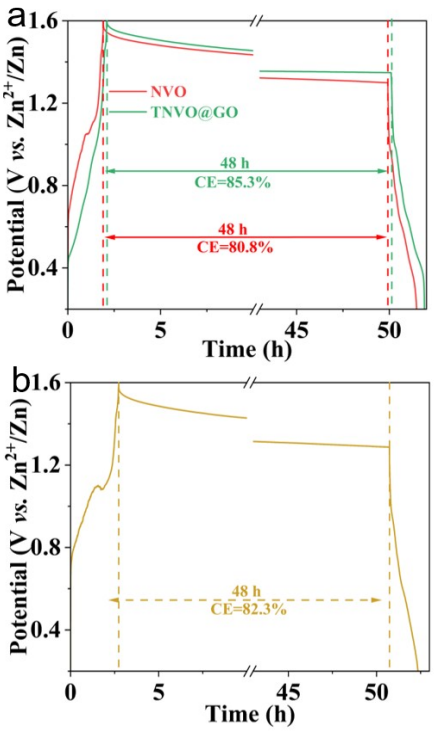


**Fig. S16.** Self-discharge test of (a) NVO and TNVO@GO and (b) TNVO.

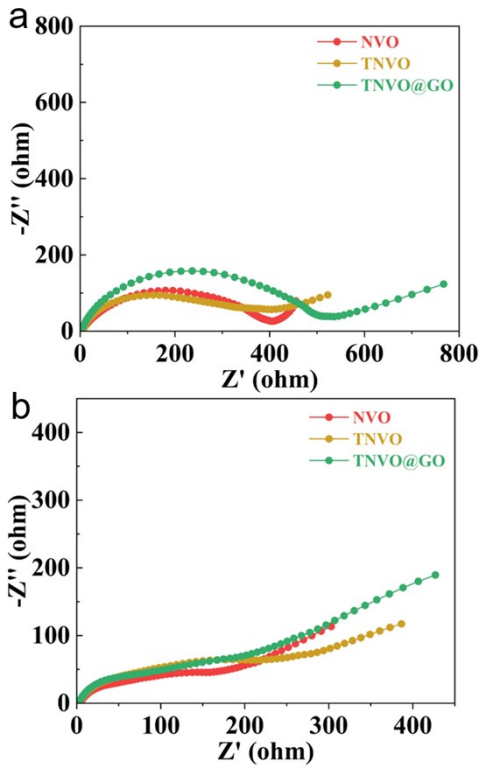


**Fig. S17.** Nyquist diagram (a) before and (b) after cycling.

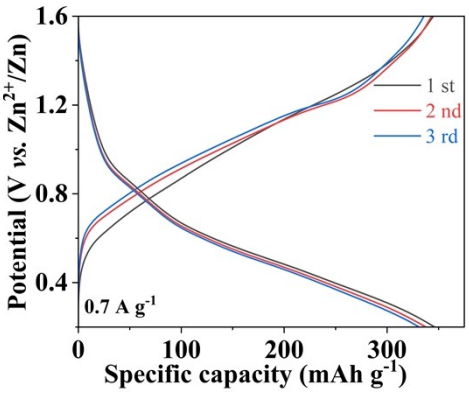


**Fig. S18.** The GCD of TNVO@GO soft pack battery.

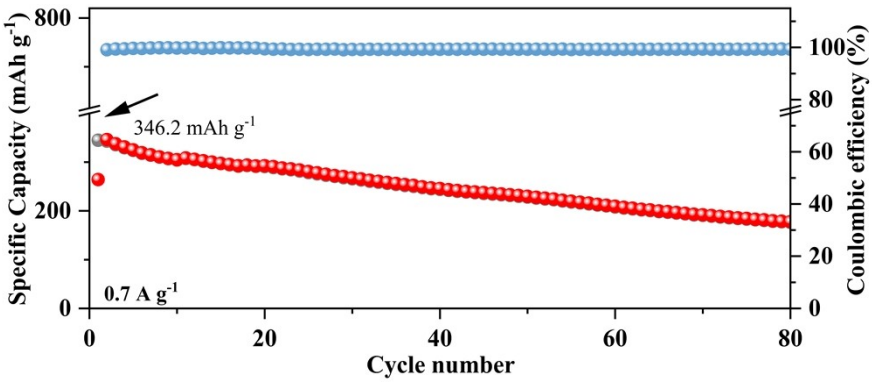


**Fig. S19.** Long cycling performance of TNVO@GO soft pack battery at 0.7 A $g^{-1}$.


**Fig. S20.** The open circuit voltage of TNVO@GO soft pack battery at135° bending states.

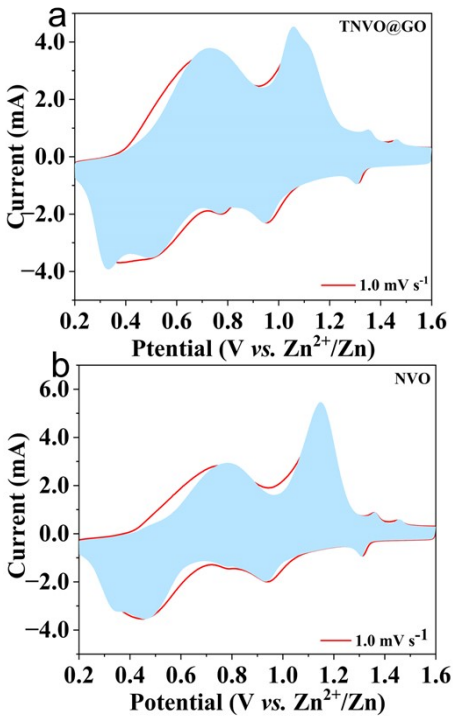


**Fig. S21.** Schematic diagram of pseudocapacitance contribution of (a) TNVO@GO and (b) NVO at 1.0 mV $s^{-1}$.

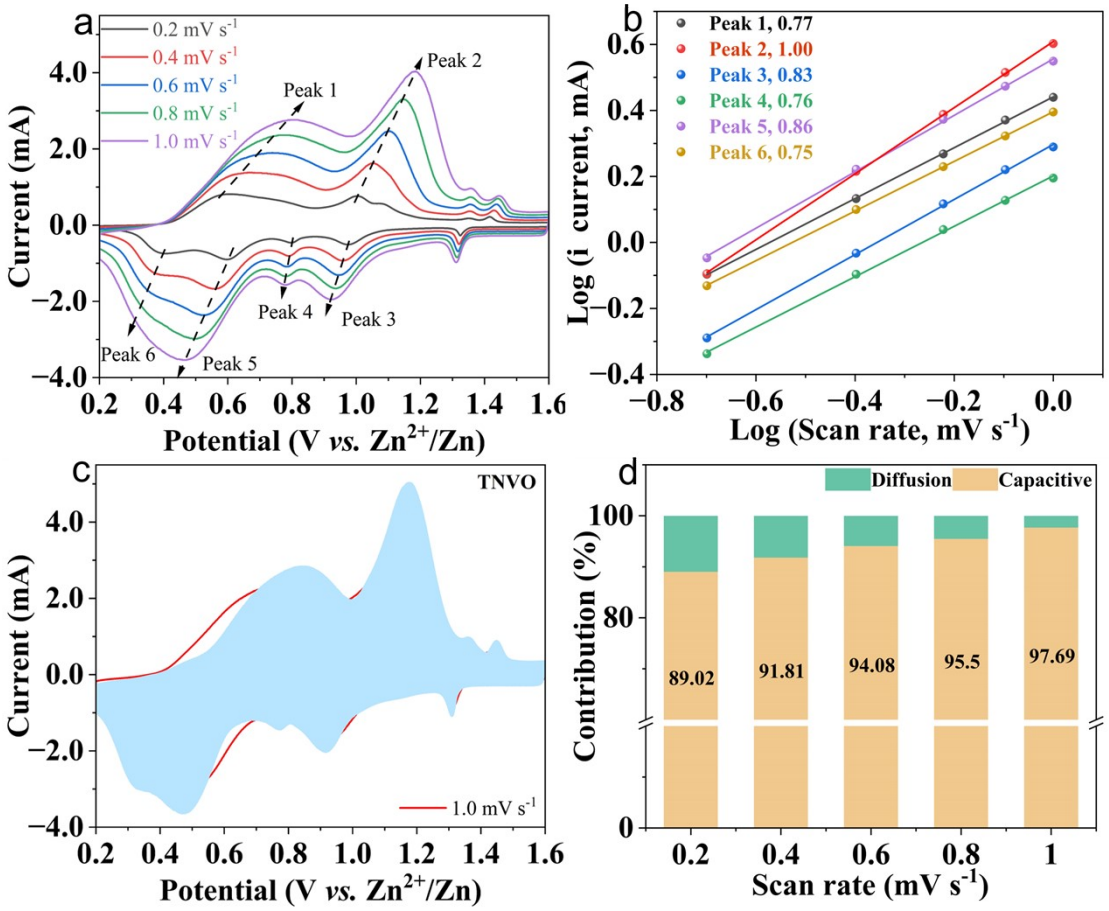


**Fig. S22.** (a) CV curves at various scan rates of TNVO. (b) The log (peak current) *vs.* log (scan rate) plot for each redox peak of TNVO. (c) Schematic diagram of pseudocapacitance contribution of TNVO at 1.0 mV $s^{-1}$. (d) Bar diagram for the contribution ratio between capacitive-controlled capacities and diffusion-controlled capacities for various scan rates of TNVO.

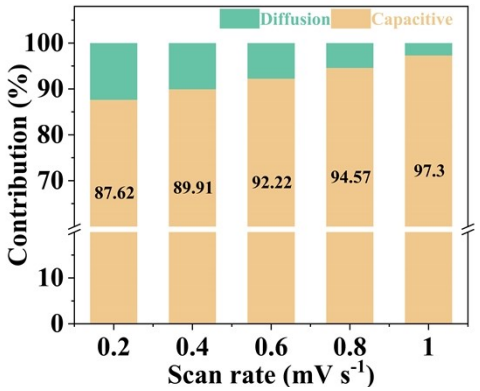


**Fig. S23.** Bar diagram for the contribution ratio between capacitive-controlled capacities and diffusion-controlled capacities for various scan rates of NVO.

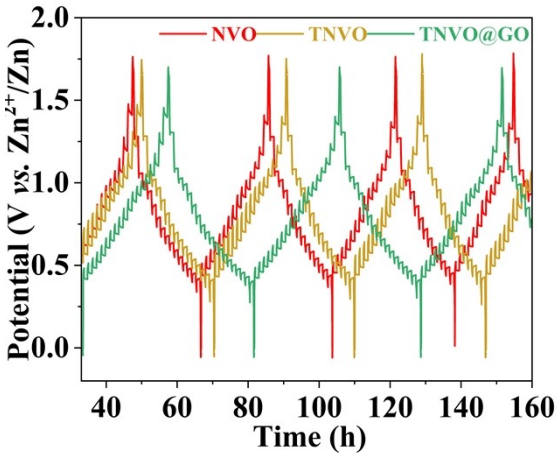


**Fig. S24.** Charge and discharge GITT curves of NVO, TNVO, and TNVO@GO at the current density of 0.1 A $g^{-1}$.

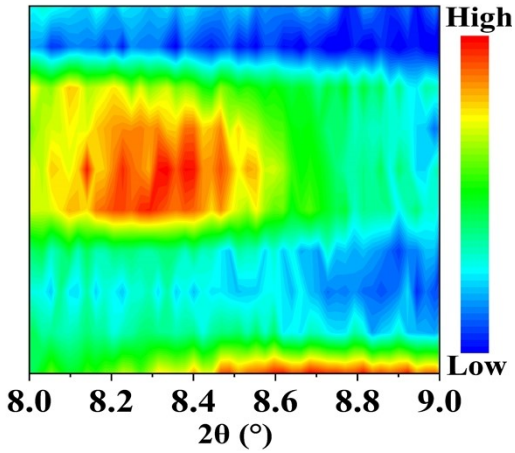


**Fig. S25.** Partial *ex-situ* XRD pattern of TNVO@GO (2θ = 8-9°).

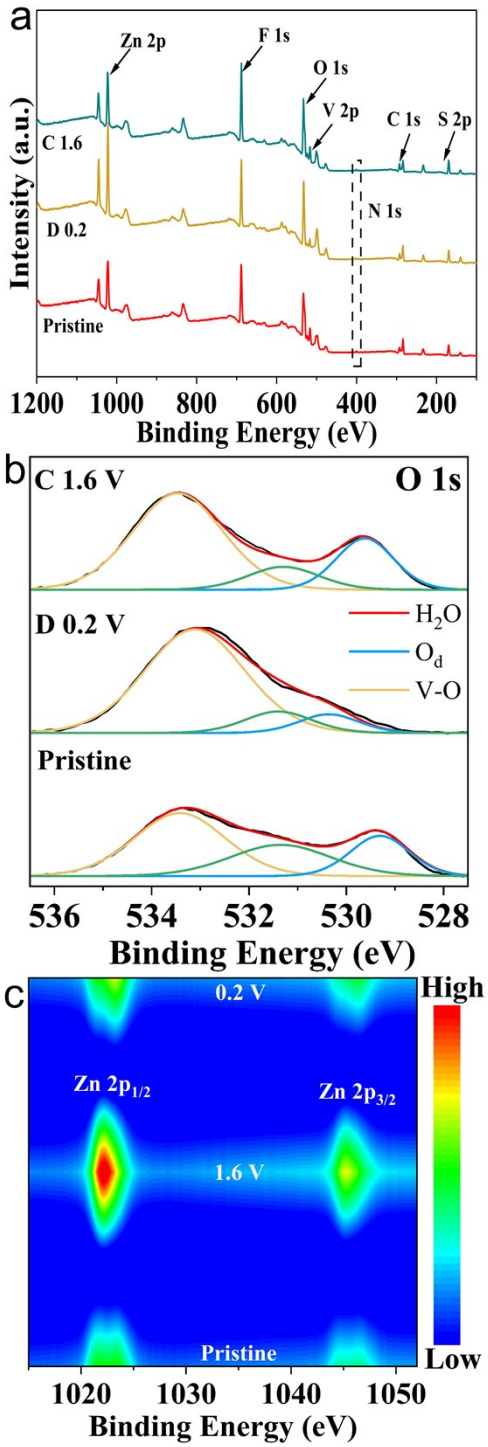


**Fig. S26.** (a) Ex-*situ* XPS survey spectrum in the fully charged and discharged states of TNVO@GO electrodes. *Ex-situ* XPS spectra of (b) O 1s and (c) Zn 2p of TNVO@GO electrodes.

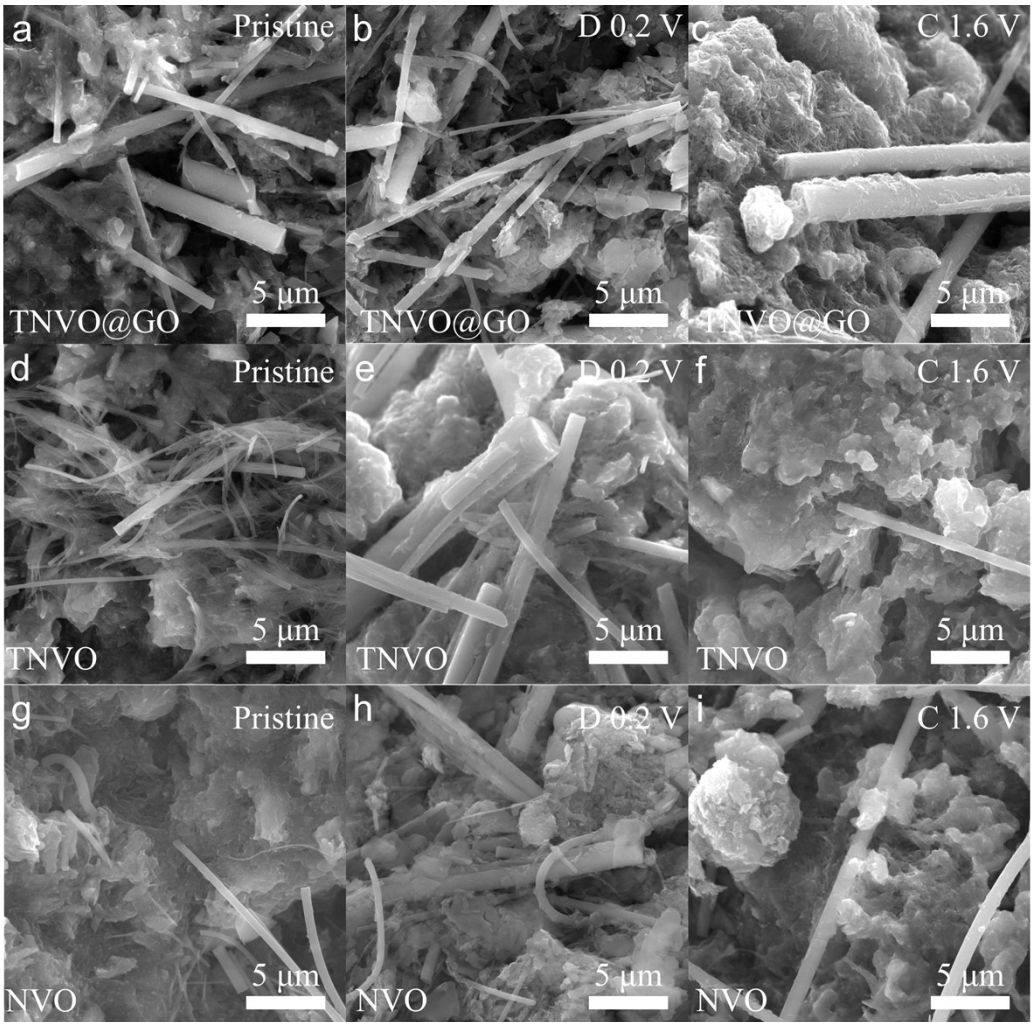


**Fig. S27.** Ex-*situ* SEM images of NVO, TNVO and TNVO@GO in the fully charged and discharged states.

**Table S1.** Atomic occupany table

| label | elem | mult | x | y | z | frac | Uiso |
|---|---|---|---|---|---|---|---|
| V1 | V+3 | 4 | 0.93 | 0 | 0.167 | 1 | aniso |
| V2 | V+3 | 4 | 0.229 | 0 | 0.174 | 1 | aniso |
| O1 | O-2 | 4 | 0.389 | 0 | 0.146 | 1 | aniso |
| O2 | O-2 | 4 | 0.082 | 0 | 0.11 | 1 | aniso |
| O3 | O-2 | 4 | 0.758 | 0 | 0.104 | 1 | aniso |
| O4 | O-2 | 4 | 0.954 | 0 | 0.355 | 1 | aniso |
| O5 | O-2 | 4 | 0.212 | 0 | 0.365 | 1 | aniso |
| N1 | N | 4 | 0.61 | 0 | 0.49 | 0.5 | aniso |
| O6 | O-2 | 4 | 0.61 | 0 | 0.49 | 0.5 | aniso |

**Table S2.** Comparison of energy density of TNVO@GO cathode with other reported aqueous cathodes.

| Eletrode materials | power density ($W\ kg^{-1}$) | energy density ($Wh\ kg^{-1}$) | Reference |
|---|---|---|---|
| NVO-300 | 209 | 245 | [37] |
| $(NH_4)_{0.78}V_4O_{10-x}\cdot 1.49H_2O$ | 398 | 184 | [38] |
| $(NH_4)_2V_{10}O_{25}\cdot 8H_2O$ | 200 | 280 | [39] |
| CVO | 53 | 267 | [40] |
| $VO_2$ | 139 | 232 | [41] |
| CaVO | 206 | 329 | [42] |
| $Cu_3V_2O_7(OH)_2\cdot 2H_2O$ | 96 | 228 | [43] |
| $V_2O_x@V_2CT_x$ | 38 | 228 | [44] |
| Zn/Mn-MOF-74 | 108 | 277 | [45] |
| a-ZVO | 36 | 116 | [46] |
| HAVO-$FeMo_6$-50 | 203 | 304 | [47] |
| NVO | 381 | 321 | [48] |
| TNVO@GO | 140 | 314 | This work |